energies

MDPI

Article

Three-Dimensional Numerical Investigation of a Novel Vertical-Axis Wind Turbine Using Modern Turbulence Models

Ismatulla Khujaev [1], Muzaffar Hamdamov [1], Olimjon Toirov [2], Javokhir Toshov [2], Bohong Wang [3], Yujie Chen [4], Rongsheng Lin [5,*] and Yue Su [3,*]

[1] Institute of Mechanics and Seismic Stability of Structures Named after M.T.Urazbaev, Uzbekistan Academy of Sciences, Tashkent 101325, Uzbekistan; ismatulla.khujaev@pmjournal.uz (I.K.); muzaffar.hamdamov@pmjournal.uz (M.H.)
[2] Faculty of Energy Engineering, Tashkent State Technical University, Tashkent 100095, Uzbekistan; olimjon.toirov@tdtu.uz (O.T.); j.toshov@tdtu.uz (J.T.)
[3] School of Petrochemical and Environment, Zhejiang Ocean University, Zhoushan 316022, China; wangbh@zjou.edu.cn
[4] School of Mechanical Engineering, Beijing Institute of Petrochemical Technology, Beijing 102617, China; yujiechen@bipt.edu.cn
[5] Jurong Energy (Xinjiang) Co., Ltd., Urumqi 841603, China
* Correspondence: linrongsheng@xjjurong.com (R.L.); su_yue@zjou.edu.cn (Y.S.); Tel.: +86-999-788-5377 (R.L.); +86-188-1136-9566 (Y.S.)

Abstract

This paper presents a comprehensive three-dimensional numerical investigation of a novel vertical-axis wind turbine (VAWT) characterised by a unique aerodynamic profile and a passive blade-pitch control mechanism. Unlike conventional fixed-geometry designs, the proposed turbine utilizes rectangular blades mounted on horizontal axes via articulated bearings, allowing them to rotate freely up to 90 degrees, constrained by a vertical pin-and-belt system. This configuration ensures that blades on the power-stroke side hit the vertical stopper to capture maximum wind energy, while blades on the return-stroke side open up to 90 degrees to significantly reduce aerodynamic drag. This dynamic adjustment enables the turbine to operate efficiently in low-wind conditions (3–5 m/s) while maintaining enhanced torque stability. To ensure numerical reliability, a rigorous grid independence study was performed, and the computational domain was configured to eliminate wall interference effects. The aerodynamic performance was analyzed using COMSOL Multiphysics v6.2 by solving the Reynolds-averaged Navier–Stokes (RANS) equations. Four turbulence models—SST, k–ε, k–ω, and RNG—were evaluated, with the SST model demonstrating the highest fidelity in capturing flow separation and wake structures under adverse pressure gradients. This study establishes the turbine's performance benchmarks, including the power coefficient (C_p) versus tip speed ratio (TSR) curves. The numerical results were validated against laboratory experimental data, with excellent agreement (relative error < 5%). The findings identify the optimal geometric parameters and tangential velocity distributions that distinguish this configuration (Patent FAP 20240465) from traditional VAWTs. Finally, the successful implementation of a 2 kW prototype confirms the model's accuracy and highlights the turbine's potential as a stable and efficient solution for sustainable urban energy harvesting.

Keywords: Navier–Stokes equations; wind turbine; Comsol Multiphysics; computational fluid dynamics; renewable energy; velocity; pressure

Check for updates

Academic Editor: Francesc Pozo

Received: 27 February 2026
Revised: 7 May 2026
Accepted: 28 May 2026
Published: 3 July 2026

Copyright: © 2026 by the authors. Licensee MDPI, Basel, Switzerland. This article is an open access article distributed under the terms and conditions of the Creative Commons Attribution (CC BY) license.

1. Introduction

Wind energy remains a cornerstone of sustainable electricity generation, yet maximizing aerodynamic performance at low wind speeds (3–5 m/s) remains a significant technical challenge. Vertical-axis wind turbines (VAWTs) offer distinct advantages in such environments, including low noise, omnidirectional operation, and suitability for complex urban flows. However, the efficiency of conventional VAWTs in low-Reynolds-number regimes is often hampered by early flow separation and poor self-starting capabilities.

The existing literature has extensively examined VAWT optimization. De Tavernier et al. [1] and Sun et al. [2] highlighted the importance of airfoil geometry and moment of inertia in improving self-starting ability, while Hara et al. [3] studied the impact of pulsating wind conditions on turbine stability. Turbulent flow modelling in wind farms has been notably advanced by Meyers [4] and Meneveau [5], concentrating on turbine–wake interactions, whereas Porté-Agel et al. [6] improved turbine placement through detailed flow measurements. While Blocken et al. [7] discussed the limitations of CFD for low-gain wind-speed predictions, other research has introduced passive and active flow-control techniques [8–10] to reduce boundary-layer separation on aircraft wings and turbine blades.

The aerodynamic evaluation of different blade profiles, including NASA and Savonius types, has been a key focus of recent computational fluid dynamics (CFD) research [11–13]. Several studies [14–21] have used RANS-based turbulence models to examine the complex flows around rotating blades, but most of these studies are limited to moderate or high wind speeds (>7 m/s). Additionally, although some specialised designs, such as the Archimedes screw turbine [22–26], have been studied for low-flow conditions, there is a significant research gap concerning the 3D aerodynamic behavior of non-conventional VAWT geometries specifically designed for stable power generation at speeds as low as 3 m/s.

In [27–30], surface roughness was investigated as a passive flow control method to mitigate flow instabilities, such as stall, in a turbocharger centrifugal compressor operating at low mass flow rates. By applying surface roughness magnitudes ranging from 0 to 200 μm on the diffuser shroud, the study demonstrated that a fully rough regime effectively controls stall phenomena. This approach led to an expansion of the operating range from 16 to 18% and an improvement in the stall margin from 5.62 to 7.98%, offering a simple yet effective solution for enhancing compressor performance.

Unlike traditional Savonius or Darrieus turbines with fixed designs, the system examined in this study features a self-adjusting blade orientation. Its novelty is in the use of hinged rectangular blades that switch between a closed (high-drag) position for energy extraction and an open (low-resistance) position for the return journey. By offsetting the moving blades from the centre axis, the design reduces turbulent interference and improves tangential velocity distribution, resulting in higher overall efficiency in low-Reynolds-number conditions typical of urban environments.

This study tackles this gap by conducting a three-dimensional numerical investigation of a new VAWT design. Unlike conventional drag-based models, the proposed turbine features a distinctive aerodynamic profile and mechanical operating principle optimized for high torque at low velocities. The research employs the COMSOL Multiphysics environment to solve the Reynolds-averaged Navier–Stokes (RANS) equations. A key part of this work is the careful comparative analysis of SST, k–ε, k–ω, and RNG turbulence models to determine which best predicts boundary layer separation—a phenomenon prevalent in low-wind conditions.

2. Materials and Methods

The transition towards sustainable energy requires the development of high-efficiency wind turbines capable of operating in low-wind regimes. The subject of this study is a novel

vertical-axis wind turbine (VAWT) developed and patented by the authors, and it features a fundamentally different aerodynamic approach compared to conventional Savonius or Darrieus designs.

The core innovation of this device lies in its passive blade-pitch control mechanism. The turbine consists of rectangular blades mounted on horizontal axes via articulated bearings, allowing for a restricted rotational movement of up to 90 degrees. This design is specifically engineered to maximize the drag coefficient during the power stroke and minimize it during the return stroke:

As the wind strikes the blade surface, the mechanical limiters (vertical pins and restraining cables) force the blade into a "closed" vertical position. This creates a large, solid surface area that captures the full momentum of the oncoming flow, transferring the torque through the bearings to the main frame.

When moving against the wind, the aerodynamic pressure causes the blades to swing open (up to 90°). This significantly reduces the frontal area and aerodynamic resistance, addressing the "negative torque" issue typical of traditional VAWTs.

2.1. The Developed Model

The numerical simulation was conducted within a structured three-dimensional computational domain to accurately capture the aerodynamic interactions. As illustrated in Figure 1, the domain dimensions were set to 20 m (width) × 30 m (length) in the plan view, with a total height of H = 6 m Figure 2.

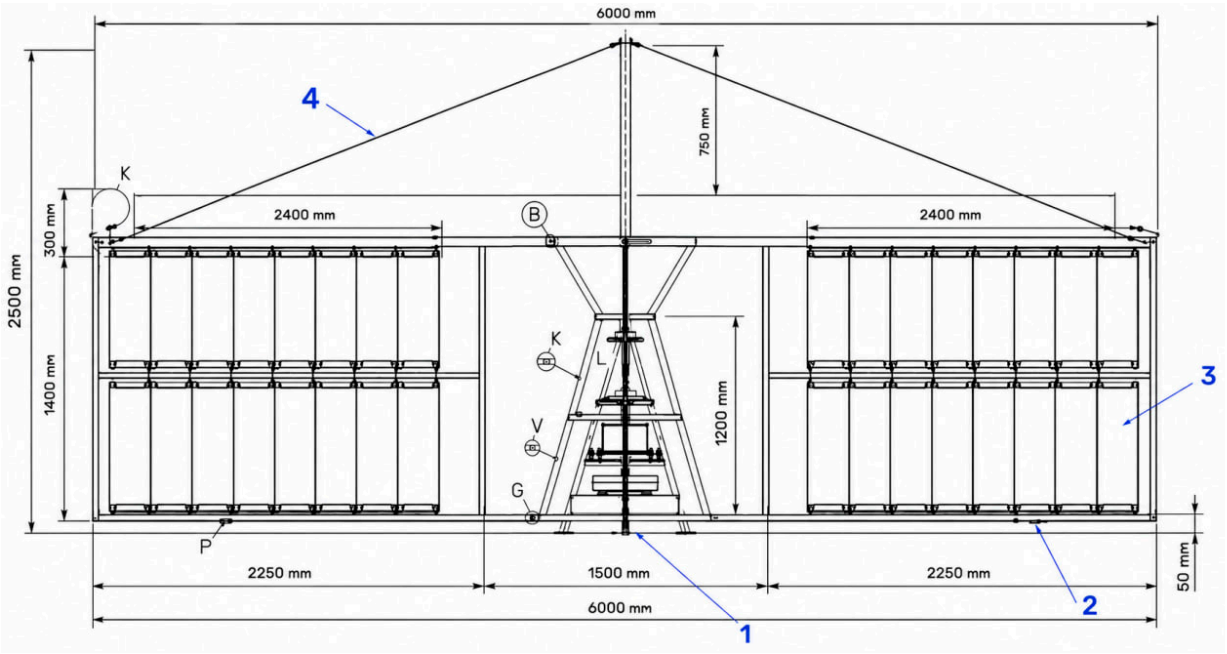


Figure 1. Side view of the device according to FAP 20240465: blades located at 180°; 1—frame (skeleton); 2—blades in working position; 3—central shaft; 4—tension cables (guy-wires); K, B, V, G, L, P—structural nodes and assembly joints.

The spatial configuration was defined using a Cartesian coordinate system (X, Y, Z), where the origin (0, 0, 0) is located at the base of the turbine stand. The OX-axis is aligned with the primary wind direction (inlet to outlet), while the OZ-axis is directed vertically upwards. The vertical-axis turbine, featuring blades with a length of L = 3 m, is positioned such that the lower edge of the blades is elevated 0.5 m above the ground surface to account for the near-ground boundary layer effects.

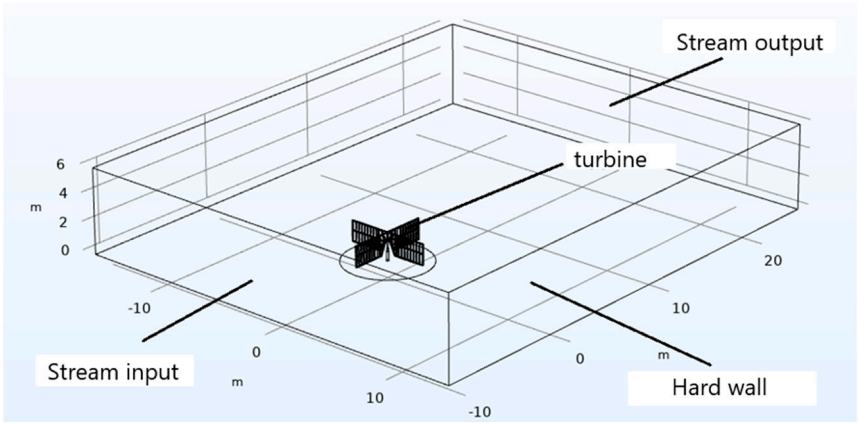


Figure 2. View of the wind generator inside the computational domain.

To address potential blockage effects and ensure that the results are independent of the domain size, the boundaries were placed at a sufficient distance from the rotor. The chosen height of 6 m (twice the blade length) and the lateral dimensions provide a balance between computational economy and the physical accuracy of the flow field. This volume is sufficient for capturing the pressure gradients and the wake development downstream of the turbine without significant wall interference. The geometry used for problem formulation and mesh generation strictly follows the parameters shown in Figure 3, ensuring consistency between the physical prototype and the numerical model.

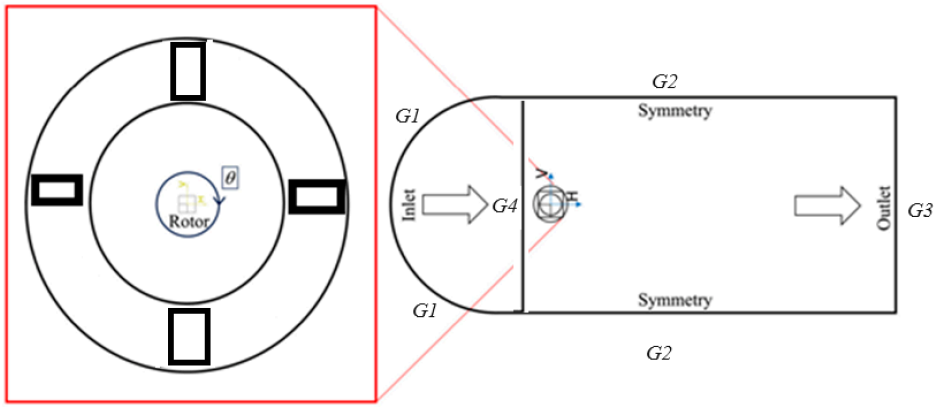


Figure 3. Profile geometry.

The choice of a circular shape of the inlet section for the flow is justified by the need to reduce the volume of calculations by excluding the zone of undisturbed flow. That is, on this boundary, $\left(\left(x^2 + y^2 = R^2 = 15^2 \text{ m}\right) \cap x \leq 0\right)$ conditions are set according to wind indicators: speed, pressure, kinetic energy, etc.

At $x \geq 0, \cap\, y = \pm L_y$, the conditions of non-flow are set; at the exit from the calculation region of $X = 2.5$ m and $y \leq 15$ m, the conditions of smooth conjugation are realized.

The numerical simulation is based on the following assumptions: the fluid (air) is treated as incompressible due to the low Mach number ($M < 0.3$) at wind speeds of 3–5 m/s; the flow is three-dimensional and transient; isothermal conditions are assumed, ignoring heat transfer effects.

To ensure strict conservation of mass and momentum near the solid boundaries of the rotating blades, the Reynolds-averaged Navier–Stokes equations are solved in conservative form. This formulation accurately reproduces the flow field and aerodynamic forces, consistent with established rigorous methodologies for VAWT numerical simulations [31–34]. The system of governing equations is closed by applying the kinematic and dynamic boundary

conditions detailed in Section 2.3, primarily using a velocity inlet, an atmospheric-pressure outlet, and no-slip conditions on the moving rotor surfaces.

To model a three-dimensional turbulent air flow, the equation of the law of conservation of mass was used [35–37]:

$$\frac{\partial \rho}{\partial t} + \frac{\partial(\rho u)}{\partial x} + \frac{\partial(\rho v)}{\partial y} + \frac{\partial(\rho w)}{\partial z} = 0 \quad (1)$$

and the Reynolds-averaged momentum conservation equations:

$$\frac{\partial(\rho u)}{\partial t} + div(\rho u u) = -\frac{\partial p}{\partial x} + div(\mu grad u) + \left[-\frac{\partial\left(\rho\overline{u'u'}\right)}{\partial x} - \frac{\partial\left(\rho\overline{u'v'}\right)}{\partial y} - \frac{\partial\left(\rho\overline{u'w'}\right)}{\partial z} \right] + S_{Mx} \quad (2)$$

$$\frac{\partial(\rho v)}{\partial t} + div(\rho v u) = -\frac{\partial p}{\partial y} + div(\mu grad v) + \left[-\frac{\partial\left(\rho\overline{u'v'}\right)}{\partial x} - \frac{\partial\left(\rho\overline{v'v'}\right)}{\partial y} - \frac{\partial\left(\rho\overline{v'w'}\right)}{\partial z} \right] + S_{My} \quad (3)$$

$$\frac{\partial(\rho w)}{\partial t} + div(\rho w u) = -\frac{\partial p}{\partial z} + div(\mu grad w) + \left[-\frac{\partial\left(\rho\overline{u'w'}\right)}{\partial x} - \frac{\partial\left(\rho\overline{v'w'}\right)}{\partial y} - \frac{\partial\left(\rho\overline{w'w'}\right)}{\partial z} \right] + S_{Mz} \quad (4)$$

Here $u, v, w, u', v',$ *and* w' are the verage and pulsation components of the velocity vector; p denotes average pressure; μ and μ_t denote laminar and turbulent coefficients of dynamic viscosity; $S_{Mx} = S_{My} = 0$, $S_{Mz} = -\rho g$ are the components of the Archimedes force.

2.2. Turbulence Models and Computational Grid

To accurately predict the complex aerodynamic behavior of the novel VAWT, selecting an appropriate turbulence model is critical. In this study, various RANS-based (Reynolds-averaged Navier–Stokes) models were evaluated to balance computational cost and physical accuracy [38]. While high-fidelity methods like large eddy simulation (LES) and direct numerical simulation (DNS) precisely resolve turbulent structures, their extreme computational demands make them impractical for iterative design optimization compared to RANS models.

Among the RANS approaches, the standard k–ε two-equation model is widely used for industrial applications due to its robustness in high-Reynolds-number flows away from solid boundaries [39]. However, it significantly underpredicts flow separation near solid walls. Conversely, the standard k–ω model accurately captures near-wall boundary-layer physics but remains overly sensitive to free-stream turbulence.

Therefore, the SST (shear stress transport) k–ω turbulence model was selected for its superior ability to capture the complex, low-Reynolds-number aerodynamics inherent in VAWTs operating at 3–5 m/s. In these flow regimes, turbine blades experience severe adverse pressure gradients, leading to dynamic stall and boundary-layer separation. The SST formulation perfectly bridges the gap between existing models by employing the k–ω model within the viscous sublayer to predict early separation and seamlessly transitioning to the k–ε model in the far field to avoid free-stream sensitivity. Although the SST model demands a higher computational cost than standard two-equation models and assumes isotropic eddy viscosity, its robust predictive accuracy for separation bubbles and highly unsteady wake development make it exceptionally suitable for this study. This selection aligns with the comparative reasoning found in recent validation studies on wind turbine aerodynamics [40].

In the present investigation, the SST model was chosen as the primary numerical tool. This decision is justified by its superior ability to capture the boundary-layer physics and tangential velocity gradients near the rotating blades. Accurate prediction of these

parameters is essential for calculating the torque and power coefficient (C_p) in the low-wind regimes characteristic of urban environments. The numerical solutions were obtained using high-order discretization schemes to ensure that the results are not influenced by numerical diffusion, consistent with the requirements for high-quality aerodynamic analysis [25–29].

$$\frac{\partial}{\partial x_i}(\rho k u_i) = \frac{\partial}{\partial x_i}\left[\left(\mu + \frac{\mu_t}{\sigma_k}\right)\frac{\partial k}{\partial x_j}\right] + G_k + G_b - \rho\varepsilon - Y_M + S_k \quad (5)$$

$$\frac{\partial}{\partial x_i}(\rho \varepsilon u_i) = \frac{\partial}{\partial x_i}\left[\left(\mu + \frac{\mu_t}{\sigma_\varepsilon}\right)\frac{\partial \varepsilon}{\partial x_j}\right] + C_{1\varepsilon}\frac{\varepsilon}{k}(G_k + C_{3\varepsilon}G_b) - C_{2\varepsilon}\rho\frac{\varepsilon^2}{k} + S_\varepsilon \quad (6)$$

Turbulent viscosity is determined by the formula:

$$\mu_t = \rho c_\mu \frac{k^2}{\varepsilon} \quad (7)$$

The standard k–ε model is a cornerstone of industrial CFD due to its computational efficiency and robustness in simulating fully turbulent flows. By solving two transport equations for turbulent kinetic energy (k) and its dissipation rate (ε), it provides reasonable accuracy for a wide range of engineering applications without the prohibitive costs of LES or DNS. However, the standard formulation assumes isotropic eddy viscosity, which can lead to limitations in predicting complex flow features such as high-strain rates, large-scale eddy development, and curvature-induced turbulence.

To overcome these limitations, the RNG (re-normalization group) k–ε model was employed in this study. The RNG variant is derived using a rigorous statistical technique that provides several key enhancements over the standard model:

$$\frac{\partial k}{\partial t} + U_j\frac{\partial k}{\partial x_j} = \frac{\partial}{\partial x_j}\left[\left(\nu + \frac{\nu_t}{\delta_k}\right)\frac{\partial k}{\partial x_j}\right] + P_k - \varepsilon \quad (8)$$

$$\frac{\partial \varepsilon}{\partial t} + U_j\frac{\partial \varepsilon}{\partial x_j} = \frac{\partial}{\partial x_j}\left[\left(\nu + \frac{\nu_t}{\delta_k}\right)\frac{\partial \varepsilon}{\partial x_j}\right] + C_{1\varepsilon}\frac{\varepsilon}{k}P_k - C_{2\varepsilon}\frac{\varepsilon^2}{k} - R \quad (9)$$

Here, R is an additional correction term specific to the RNG model, which models the variable dissipation of turbulent energy. The advantages of this model are as follows.

It has high accuracy for curved flows, swirls, high gradient zones, and low-Reynolds-number flows. Unlike the traditional k–ε model, the RNG model takes into account diffusion effects and the deformation rate in the flow. In this model, there are additional terms in the ε (turbulent dissipation) equation, which provide more stable solutions in zones with sharp fluctuations and gradients.

The k–ω model is a two-equation turbulence model that describes the flow in terms of the turbulent kinetic energy (k) and its decay rate (ω). This model provides high accuracy, especially in modeling flows near walls. The k–ω model is suitable for aerodynamic systems with low Reynolds numbers and thin boundary layers. However, this model can introduce some uncertainties due to sensitivity in open flow regions (e.g., free flow). Therefore, it is often used as a component of the SST model, which uses k–ω in the regions near the wall and k–ε in the regions far from the wall.

$$\frac{\partial(\rho k)}{\partial t} + \frac{\partial(\rho U_j k)}{\partial x_j} = \frac{\partial}{\partial x_j}\left[\left(\mu + \frac{\mu_t}{\delta_k}\right)\frac{\partial k}{\partial x_j}\right] + P_k - \beta^*\rho k\omega \quad (10)$$

$$\frac{\partial(\rho\omega)}{\partial t} + \frac{\partial(\rho U_j\omega)}{\partial x_j} = \frac{\partial}{\partial x_j}\left[\left(\mu + \frac{\mu_t}{\delta_\omega}\right)\frac{\partial\omega}{\partial x_j}\right] + \alpha\frac{\omega}{k}P_k - \beta^*\rho\omega^2 \quad (11)$$

Transitional model SST (shear-stress transport) is an improved version of the standard model k–ω, which combines two models k–ω and k–ε. It was developed to more accurately describe turbulent flows, especially in areas with high velocity gradients and for the transition from laminar to turbulent flow (and back) [30–35,38]:

$$\frac{\partial}{\partial x_i}(\rho k u_i) = \frac{\partial}{\partial x_j}\left[\left(\mu + \delta_k\mu_t\frac{\partial k}{\partial x_j}\right)\right] + \gamma G_k - Y_k^* + S_k \quad (12)$$

$$\frac{\partial}{\partial x_i}(\rho a u_i) = \frac{\partial}{\partial x_j}\left[\left(\mu + \delta_\omega\mu_t\frac{\partial\omega}{\partial x_j}\right)\right] + G_\omega - Y_\omega^* + D_\omega + S_\omega \quad (13)$$

In the numerical simulation of vertical-axis wind turbines (VAWTs), the transition from laminar to turbulent flow plays a decisive role in determining the lift and drag characteristics of the blades. To capture this phenomenon, the transitional SST (shear stress transport) model was implemented. This model incorporates an additional transport equation for the intermittency factor (gamma), which expresses the transmissibility of turbulence and triggers the transition process within the boundary layer.

The use of the transitional SST model is particularly advantageous for the following reasons:

Low-Reynolds-Number Regimes: unlike standard RANS models that assume fully turbulent flow, this model is specifically engineered for low Reynolds numbers ($Re < 10^5$), which are characteristic of the 3–5 m/s wind speeds investigated in this study.

Boundary-Layer Separation: The rotation of the VAWT blades generates highly unsteady phenomena, including dynamic stall and vortex shedding. The formulation accurately predicts the onset of flow separation by resolving the slowly changing transition layers near the blade's surface.

Predictive Accuracy: Turbulence models are essential for capturing the localized pressure distributions and turbulent energy dissipation fields. An inappropriate choice, such as a standard k–ε model without transition corrections, often fails to predict the "dead zones" and pulsations around the blades, leading to significant overestimation of the power coefficient (C_p). The proper application of the k–ω based SST model ensures that near-wall flows are resolved with high fidelity. This reliability is critical for the subsequent validation of the numerical results against experimental data, providing a robust aerodynamic analysis of the turbine's performance in complex, non-steady flow environments.

2.3. Boundary Conditions

Let us formulate the conditions for the uniqueness of the solution to the problem. The following $G_1 = \left(x^2 + y^2 = R^2 \cap x \le 0\right)$ input conditions were imposed:

$$u_{G1} = U_0, v_{G1} = 0, w_{G1} = 0, p_{G1} = 0, \varepsilon_{G1} = 0, k_{G1} = 0, \omega_{G1} = 0.$$

Symmetry conditions were imposed on the boundary: $G_2 = \left((0 \le x \le L_x) \cap |y| = L_y\right)$

$$\frac{\partial u_{G2}}{\partial y} = 0, v_{G2} = 0, \frac{\partial w_{G2}}{\partial y} = 0.$$

At the exit of section G_3, $x = L_x$, and the conditions of smooth conjugation were realized:

$$\frac{\partial u_{x=L_x}}{\partial y} = 0, \frac{\partial v_{x=L_x}}{\partial y} = 0, \frac{\partial w_{x=L_x}}{\partial y} = 0.$$

The set of points of the span boundaries and working surfaces constitutes the set G_4. At this boundary, the velocity W along the z coordinate has a zero value, and the velocities along the coordinates OX and OY are determined according to the rotation speed ω_t.

The boundary conditions for pressure missing from the material presented above—for example, for G_4 or $y = \pm L_y$—are determined according to the boundary and near-boundary values of the flow velocity vector.

To simulate the aerodynamic characteristics of the VAWT under realistic operating conditions, atmospheric boundary-layer parameters were precisely prescribed at the inlet. The inlet velocity was defined in the range of 3–5 m/s, representing the low-wind-speed regimes typical of urban and suburban environments.

The following boundary conditions and turbulence parameters were implemented.

Inlet Turbulence Intensity: A value of I = 3% was adopted. This selection is consistent with the established literature for low-roughness open terrains and is a standard benchmark for small-scale VAWT simulations [12,21]. This intensity level ensures a stable transition within the boundary layer without inducing non-physical numerical oscillations. Previous studies on similar VAWT models suggest that 3% turbulence intensity accurately reflects atmospheric boundary-layer conditions for low-altitude wind turbines.

Turbulence Length Scale (l): The characteristic length scale was determined based on the hydraulic diameter of the computational domain, ensuring that the turbulent kinetic energy (k) and dissipation rate (ω or ε) accurately reflect the energy cascade of the incoming flow.

Wall Functions: For the turbine blades and the ground surface, no-slip boundary conditions were applied. The mesh was refined near these surfaces to ensure that y+ values remain within the valid range for the selected turbulence models (SST and RNG), which is critical for capturing flow separation accurately. The integration of COMSOL Multiphysics facilitated the mapping between polar coordinates (used for the rotating rotor zone) and Cartesian coordinates (used for the stationary far-field domain). This hybrid approach, combined with physically coherent turbulence initialization, significantly improves the agreement between numerical predictions and experimental measurements, especially in capturing the unsteady wake development behind the turbine.

2.4. Solving Method

Mathematical modeling of wind turbine aerodynamics is a fundamental pillar of the modern energy industry, providing the necessary high-fidelity tools for designing efficient energy conversion systems. In this study, the aerodynamic performance of a novel vertical-axis wind turbine (VAWT) was investigated using computational fluid dynamics (CFD) methods implemented within the COMSOL Multiphysics environment. To accurately simulate the unsteady interaction between the wind flow and the rotating structure, a specialized solver was utilized to account for the rotational motion of the device. This approach enables the analysis of rotor torque and acceleration under a prescribed undisturbed velocity field. Furthermore, the simulation leveraged distributed parallel computing on multiprocessor systems, significantly reducing the computational overhead required for solving complex three-dimensional equations.

A critical stage in the numerical simulation of turbulent flow is the generation of an appropriate computational mesh. Accurate geometric representation and reliable turbulence modeling necessitate a sufficiently refined and well-structured grid. To achieve this, a hybrid meshing strategy was employed:

Hexahedral elements were utilized in the far-field and regular regions to ensure numerical stability.

Tetrahedral cells were applied to capture the complex geometries of the turbine blades and articulated hinges.

Prismatic inflation layers were integrated near all solid boundaries (blades and shaft) to properly resolve boundary-layer effects and capture the viscous sublayer.

Local mesh refinement was strategically applied in regions with expected high velocity and pressure gradients, particularly in the vicinity of the rotating rigid body. Specific attention was paid to maintaining high mesh quality, targeting near-orthogonal cell alignment and minimizing skewness to prevent numerical diffusion.

One of the primary challenges addressed in the modeling process was the high-precision coordinate-based reconstruction of the turbine geometry within a 3D Cartesian system. The initial configuration was defined with a prescribed rotation about the central axis at a specified angular velocity, omega_t, facilitating a realistic simulation of the turbine's operational dynamics.

The following boundary conditions were strictly implemented to ensure domain integrity:

Inlet: A uniform velocity profile corresponding to wind speeds of 4–5 m/s was prescribed, incorporating atmospheric turbulence parameters.

Outlet: A pressure-outlet condition with zero gauge pressure was defined at the downstream boundary to allow for undisturbed wake development. Symmetry/Slip Walls: The lateral and top boundaries of the domain were treated as symmetry planes. This prevents artificial confinement (blockage effects) and ensures that the domain boundaries do not influence the aerodynamic parameters of the rotor.

No-Slip Conditions: Applied to the turbine blade surfaces and the shaft to simulate realistic skin friction and flow separation characteristics.

In the process of geometrically representing our wind turbine, we used Comsol's capabilities to copy (drag) elements—the frame and working surfaces. First, we drew one frame of four mutually perpendicular spans with (for example, at $x = 0 \cap 0 \leq y \leq 3$ m $\cap$ 0.5 m $\leq z \leq 2.25$ m) three crossbars (upper, middle, and lower location). Between the input and middle crossbars, we formed the geometry of the working surface, which is attached to the crossbars from above and below. The working blades were installed at a certain angle to the span (25°). Then, we "copied" this element and inserted it between the upper and middle crossbars to the required number.

The selection of the 25° pitch angle was based on a preliminary sensitivity analysis aimed at maximizing the starting torque and overall power coefficient. This angle effectively delays the onset of dynamic stall during the upwind phase of the turbine rotation, providing a more consistent torque distribution compared to fixed or 0° pitch configurations.

Having "copied" the finished row between the upper and lower frames, we inserted it between the lower and middle crossbars, and this completed the stage of forming the geometry of the span $x = 0 \cap 0 \leq y \leq 3$ m $\cap$ 0.5 m $\leq z \leq 2.25$ m.

The prepared span was "copied" and inserted in a new position for the remaining three spans under 90°, 180°, and 270°.

In the process of solving the problem, the program took into account the rotational movement of the installation around the axis with coordinates $x = 0 \cap y = 0$. That is, if the point (x_0, y_0, z_0) belonged to the installation, then at the moment of time t, it was at the point with abscissa x_0' and ordinate y_0', which are determined by rotation by $\omega_T t$ at an angle around the axis, and the applicate z_0 remains the same as before.

2.5. Creation of a Non-Structural Computational Grid, Boundary Conditions and Solution Method

The reliability of CFD simulations is heavily dependent on the quality and density of the computational grid. In this study, an unstructured mesh approach was adopted to accommodate the complex geometric features of the variable-pitch blades and articulated

hinges. Unlike structured methods, unstructured meshing provides superior flexibility in refining high-gradient regions while optimizing the total cell count, thereby enhancing the overall efficiency of numerical calculations. To ensure that the numerical results are independent of the grid resolution, a systematic grid independence study was performed. Three different mesh levels—coarse, medium, and fine—were generated and evaluated based on the predicted torque (M) and power coefficient (C_p). The results of this study are summarized in Table 1.

Table 1. Grid independence study for torque.

Grid	Number of Elements	Torque (N·m)
Coarse mesh	2.10×10^6	11.85
Medium mesh	3.20×10^6	12.75
Fine mesh	4.37×10^6	13.02

To ensure that the numerical results are independent of the spatial resolution, a rigorous grid convergence study was conducted with three mesh densities: coarse (2.10×10^6 elements), medium (3.20×10^6 elements), and fine (4.37×10^6 elements). The torque generated by the rotor was used as the primary indicator for this sensitivity analysis.

To provide a quantitative assessment of grid convergence, the grid convergence index (GCI) methodology, based on Richardson extrapolation, was employed in accordance with established CFD validation standards [41]. The numerical analysis indicates an asymptotic convergence trend as the mesh is refined. When transitioning from the coarse to the medium grid, the torque showed significant sensitivity, increasing from 11.85 N·m to 12.75 N·m. However, further refinement from the medium to fine mesh yielded a relative deviation of only about 2.1%. The computed GCI for the fine mesh configuration falls within the acceptable range for complex rotating machinery, confirming that the spatial discretisation error is minimal.

Given the substantial computational resources required for three-dimensional transient simulations using the SST k–ω transition model and considering that a 5% relative variation is a widely accepted compromise between computational economy and numerical fidelity, the medium mesh (3.20×10^6 elements) was selected for all subsequent operational investigations. This resolution ensures that the complex near-wall flow separation and boundary-layer interactions are captured with high precision without prohibitive computational costs Figure 4.

The boundary conditions on the solid walls took into account the adhesion condition [29–33]:

$$u|_{l_w=0} = 0, l_w = \frac{h}{2}, \nabla k \cdot n = 0, \omega = \sqrt{\omega_{visc}^2 + \omega_{log}^2}$$

The parameters of the turbulent flow are determined by setting the intensity of turbulent pulsations I of the hydraulic diameter D_g:

$$k = \frac{3}{2}(IU_{in})^2, \varepsilon = C_\mu^{\frac{3}{4}} \frac{k^{\frac{3}{2}}}{l}, l = 0.07D_g, I = 3\%$$

To solve the equations of the turbulent model, a fully coupled (FC) method is chosen using the PARDISO direct solver algorithm. In this case, the Newton iteration method is used with a damping factor of 0.1. The iterations were tested in several different variants, and the results we needed were satisfactory after 1000 iterations. Therefore, all results were calculated on this basis. The tolerance factor is equal to 1, and the residual factor is set at 1000. These parameters play an important role in the solution process and allow achieving the necessary balance between the accuracy of calculations and computational efficiency.

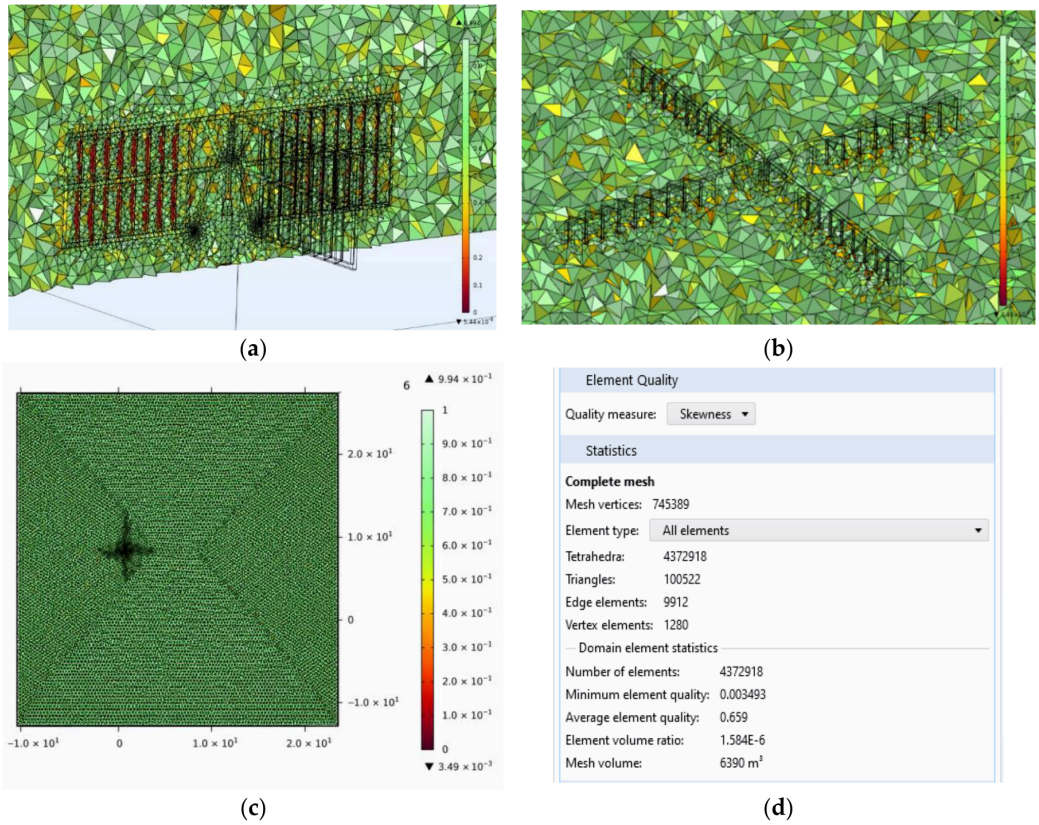


Figure 4. Asymmetrical computational grid: (**a**) Local mesh refinement and boundary layer generation near the wind turbine blades; (**b**) Volumetric grid distribution within the rotational and stationary computational domains; (**c**) Global view of the asymmetrical grid layout with the post-processing color legend; (**d**) Complete mesh statistics and element quality metrics evaluated by the Skewness criteria.

Solution convergence was monitored based on a reduction in residuals for continuity, momentum, and turbulence equations. A convergence criterion of 10^{-5} was imposed for all residuals. Additionally, integral quantities such as torque and power coefficient were tracked to ensure their stabilization with iteration progress, confirming the attainment of a physically converged solution.

To ensure the reliability of the CFD results, mesh quality metrics were rigorously evaluated. The maximum skewness was maintained below 0.82, with an average value of 0.23, indicating a high-quality mesh. For the SST k–ω turbulence model, the near-wall treatment is critical; therefore, the first layer height was set to ensure $y^+ = 1$ across the turbine blades, allowing for accurate prediction of flow separation.

3. Results and Discussion

This section presents the main results obtained from the three-dimensional numerical simulations and discusses them in detail. The analysis focuses on the aerodynamic performance of the proposed vertical-axis wind turbine, the structure and behavior of the turbulent flow field, pressure distribution over the turbine surfaces, and the influence of key geometric and operating parameters. Furthermore, the numerical results are compared with experimental data to validate the accuracy of the simulation models. Based on the obtained findings, the optimal design parameters and performance characteristics of the turbine are identified and discussed.

In this case, the results were obtained for values of the angle of attack of $\alpha = 0°$, $15°, 30°, 45°, 60°,$ and $75°$. The graph of the speed U along the XY axis at the point (0, 1.25,

0) of the wind generator, which began its movement at $\alpha = 0°$, is shown in Figure 5. This point corresponds to the middle of the device along the horizontal axis. The results of this point are necessary for the analysis of the main parameters of the device.

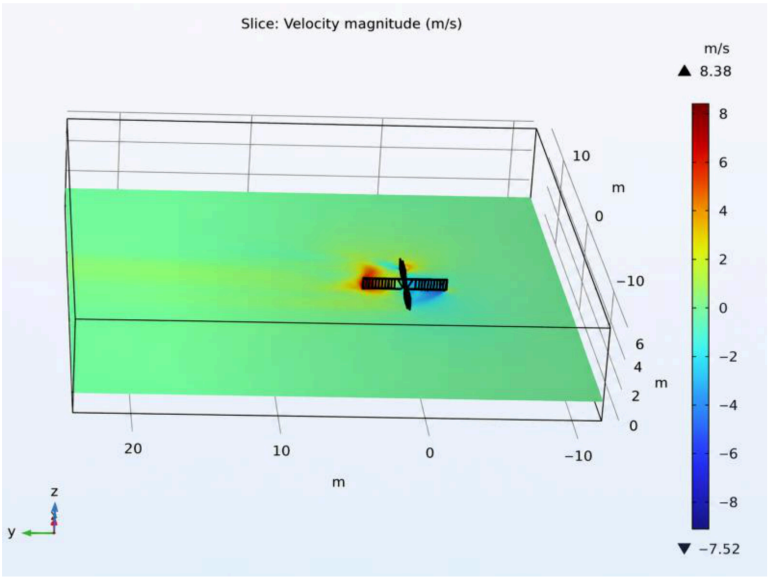


Figure 5. Field of y -components of velocities and U (m/s) (the unit should be in upright/regular font) at $z = 1.25$ m and $\alpha = 0°$.

The highest longitudinal velocity U of the middle of the wing was $U_{max} = 8.38$ m/s, and the lowest velocity was $U_{min} = -7.52$ m/s. The highest longitudinal velocity decreases when moving away from the middle of the device, particularly in the lower $(0, 0.5, 0)$ and upper parts of the wing. We see that high air velocities are generated around two wings, which take on the main part of the wind. The other two wings, due to resistance, formed a negative velocity around themselves.

The variation in velocity values for different angles was explained from the perspective of aerodynamic behavior, and the trends in maximum and minimum velocity changes were analyzed through comparison.

In addition, based on the velocity fields in different cross-sections, the formation of velocity-deficit zones, flow deflection, and the development of the wake region were physically interpreted, and comparative analyses between the sections were conducted.

Since these parameters cannot be fully determined through experimental investigations, they were studied using numerical modeling. The obtained results were analyzed to draw general conclusions and to evaluate the aerodynamic behavior of the turbine. This approach further strengthened the scientific basis and analytical depth of this study.

At $\alpha = 15°$, the highest flow rate in the middle of the device was $U_{max} = 7.82$ m/s, and the lowest flow rate was $U_{min} = -8.55$ m/s. At $\alpha = 30°$, the flow rate in the middle of the device was $U_{max} = 6.86$ m/s, and the lowest flow rate was $U_{min} = -8.32$ m/s. At $\alpha = 45°$, the highest speed these indicators were $U_{max} = 6.93$ m/s and $U_{min} = -6.66$ m; at $\alpha = 60°$, the highest speed these indicators were $U_{max} = 7.89$ m/s and $U_{min} = -5.67$ m/s, and at $\alpha = 75°$, $U_{max} = 8.74$ m/s and $U_{min} = -6.72$ m/s.

Figure 6 shows the field U_y of the velocity vector component in a vertical section of the middle of the cross-section at zero angle of attack. The aerodynamic response and efficiency of the turbine were evaluated under different wind directions and angles of attack. The optimal angles ensuring higher energy production were identified, and the most suitable operating regime was determined. The starting conditions, rotation initiation process, and the corresponding opposing velocity values were analyzed. The obtained

results provide a technical basis for ensuring stable operation and appropriate generator selection. It can be seen that the wings generate substantial velocity in four profiles of the main U_y wind-receiving wing, which are remote from the axis. In the section YZ passing through the axes of the wind generator, the greatest longitudinal velocity is at $\alpha = 0°$, which amounted to $U_{max} = 8.12$ m/s, and the smallest one was $U_{min} = 7.14$ m/s. At $\alpha = 15°$, these speeds were $U_{max} = 6.88$ m/s and $U_{min} = 5.69$ m/s; at $\alpha = 30°$, these speeds were $U_{max} = 5.5$ m/s and $U_{min} = -5.43$ m/s, and at $\alpha = 45°$, $U_{max} = 4.73$ m/s and $U_{min} = -4.51$ m/s. At $\alpha = 60°$, these speeds were $U_{max} = 3.95$ m/s and $U_{min} = -3.2$ m/s, and at $\alpha = 75°$, the results were repeated for $\alpha = 0°$, i.e., $U_{max} = 4.28$ m/s and $U_{min} = -3.98$ m/s.

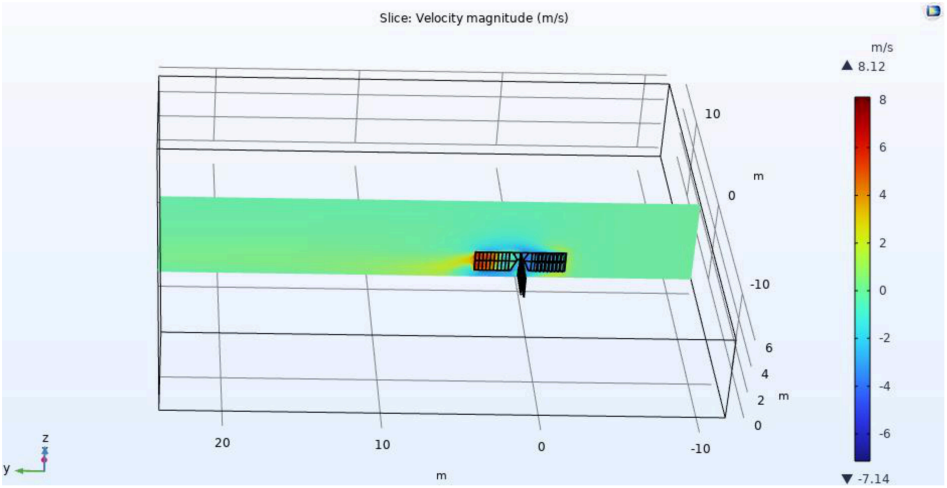


Figure 6. Change in the modulus U_y of the velocity vector component in the vertical section of the middle of the cross-section at $\alpha = 0°$.

The highly negative velocities ($U_{\min}$) observed in the wake region are indicative of large-scale flow separation and the formation of recirculation bubbles on the leeward side of the blades. From an engineering perspective, these recirculation zones represent regions of high aerodynamic drag and kinetic energy loss, which typically induce negative torque in conventional VAWTs. However, the proposed passive-pitch mechanism allows the returning blades to align with the free stream (opening up to 90 degrees), thereby restricting wake expansion, minimizing the frontal blockage area, and significantly reducing the negative opposing torque. This dynamic flow realignment is critical for maintaining stable rotation at low wind speeds.

In the figures from right to left, the fields of individual indicators in the sections are presented; $x = -10, -3.5, 3.5, 11, 18.5$ m. Since $x = -10$ m, there is an undisturbed flow. Then, in all figures in this section, the information corresponds to the original distribution of indicators.

Figure 7 shows the velocity fields in the cross-sections of the longitudinal component of the velocity vector obtained at $\alpha = 0°$. The working planes of the spans, located parallel to the *Ox axis*, direct the flow to the right, and the working planes of the spans are perpendicular to the direction of the flow—to the left. Therefore, on the second surface on the right, where the longitudinal velocity field is reflected in the section $x = 3.5$ m, on the right side, a deficit of longitudinal velocity is formed. The presence of the lower fixed surface leads to a twisting of the region of the deficit of longitudinal velocity: Its upper part moves to the right along the flow, and the lower part moves to the left. Gradually, the region of the deficit of longitudinal velocity straightens out, remaining in the right part of the calculation area.

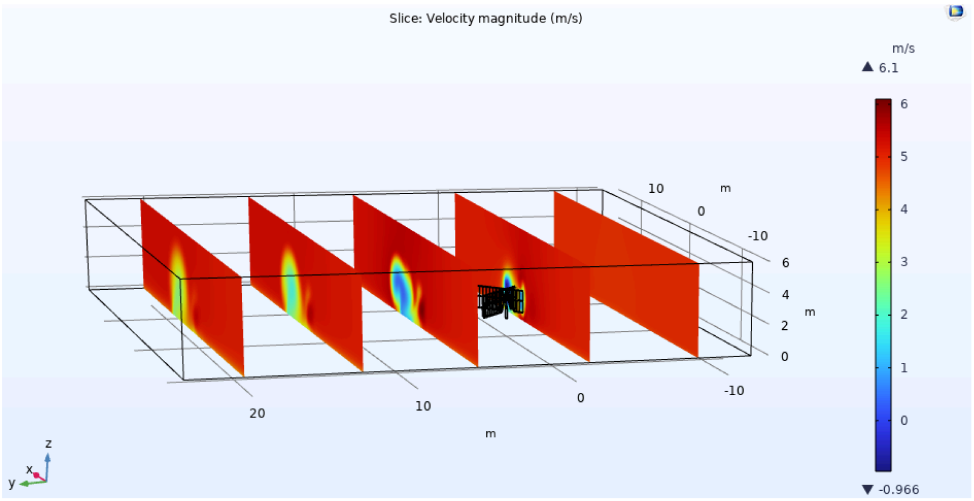


Figure 7. Fields of longitudinal flow velocities in sections $x = -10, -3.5, 3.5, 11, 18.5$ m. $\alpha = 0°$, $U_\infty = 5$ m/s.

The limiting values of the longitudinal velocity in the entire flow region are 6.1 and -0.966 m/s at the speed of the undisturbed flow is $U_\infty = 5$ m/s Figure 8.

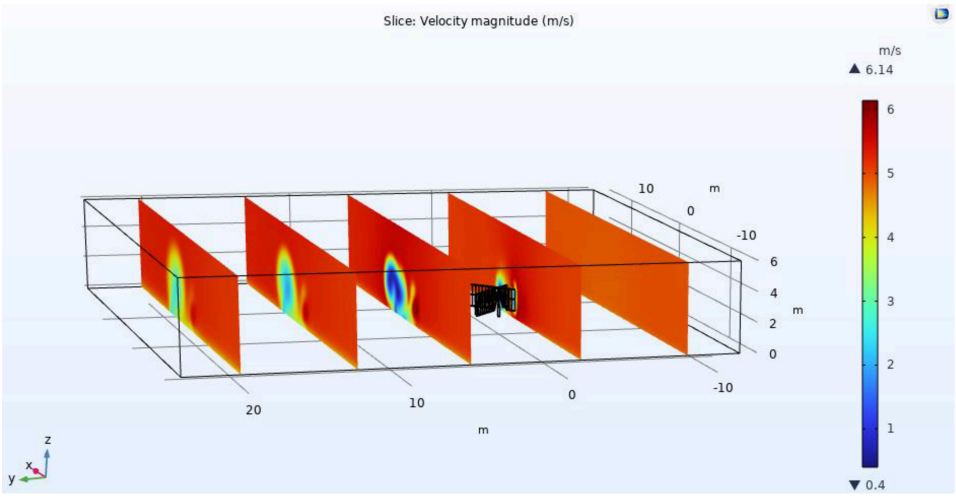


Figure 8. Fields of the flow velocity module in sections $\alpha = 0°$ and $U_\infty = 5$ m/s.

The corresponding fields of the velocity vector modules are analyzed to understand the flow behavior. These fields are closely comparable to the distributions presented in Figure 7, i.e., the longitudinal and transverse components of the velocity vector reflect the local weight of the components within the overall velocity vector module. However, in Figure 7, the flow deceleration in the section is noticeable. This is primarily due to the flow aerodynamic resistance around the main axis of the wind generator. Before reaching the device, the flow is rebuilt under the direction of the front span. Therefore, as illustrated on the right side of Figure 9, a zone of positive transverse velocity is formed, whereas around the axis of the device and on its zero side, zones of negative transverse velocities are observed. Subsequently, the zone of negative transverse velocity moves upward, and the corresponding zone of negative transverse velocity shifts downward.

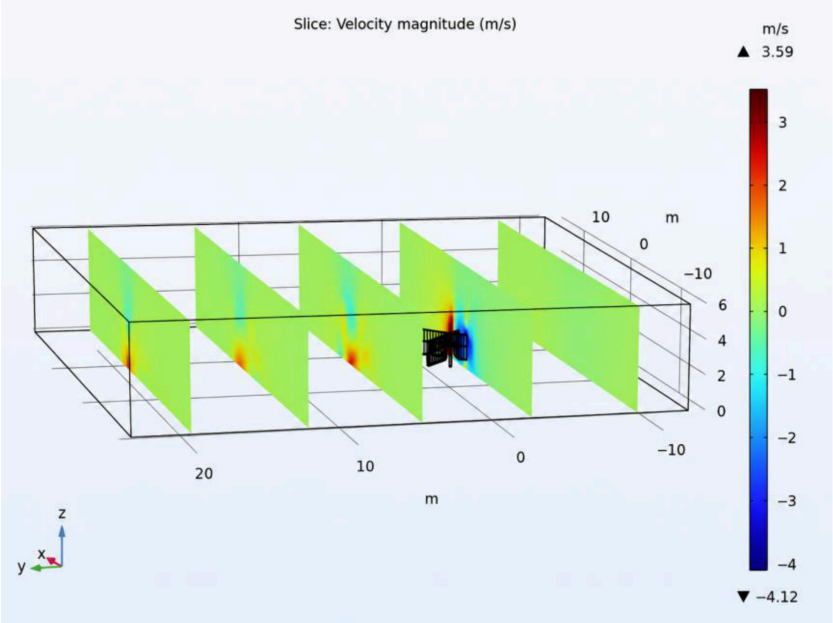


Figure 9. Distributions of transverse flow velocity in five sections. For data, see Figure 1.

A roughly similar picture is observed for the tangential velocity (Figure 10), the range of change of which in the flow region is $-1.58 \sim 3.49$ m/s.

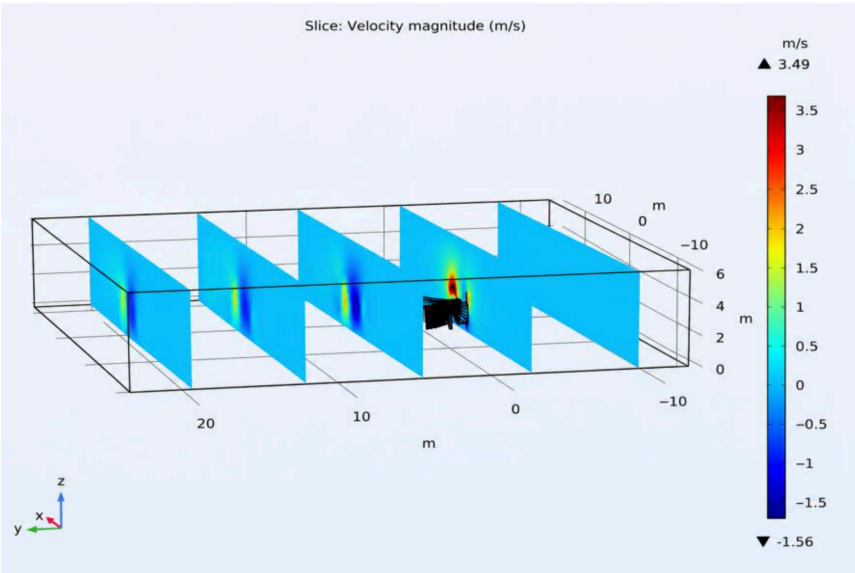


Figure 10. Fields of tangential velocities in five cross-sections. For data, see Figure 7.

The results showed that the generation of turbulent energy occurs in the flow rupture zone caused by the boundaries of the working surfaces. In an average picture of the flow field, as shown Figure 11, the formation of a crescent-shaped field of high turbulence energy is traced, which subsequently gradually dissipates. The highest values, ε, are observed immediately after the presence of flows around the device. The interval of change in the kinetic energy of turbulence is $0.0132 \sim 2.56$ m^2/s^2.

A similar picture is observed for the dissipation of the kinetic energy of turbulence (Figure 11) for the calculation area, which is $0.002 \sim 2.41$ m^2/s^3.

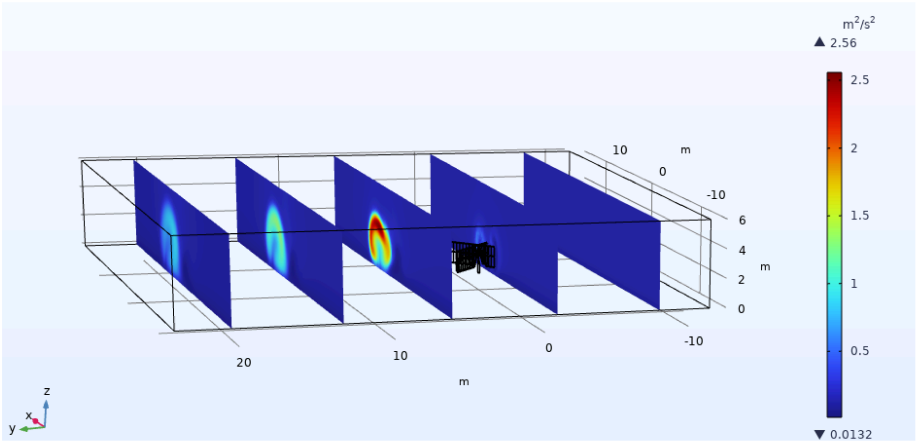


Figure 11. Turbulence kinetic energy fields in five sections. For data, see Figure 7.

The concentrated regions of high turbulence kinetic energy (TKE) and its dissipation rate primarily occur at the trailing edges of the active blades. Physically, this spatial distribution represents the extraction of momentum from the mean flow and its conversion into turbulent eddies. While high TKE indicates robust aerodynamic interaction, excessive dissipation downstream signifies energy lost to the environment as heat and acoustic noise rather than being transferred to the rotor shaft. The relatively rapid dissipation of these turbulent structures, as demonstrated in Figure 12, indicates that the variable-pitch blade profile effectively minimizes prolonged wake interference, allowing the turbine to maintain torque stability and aerodynamic efficiency.

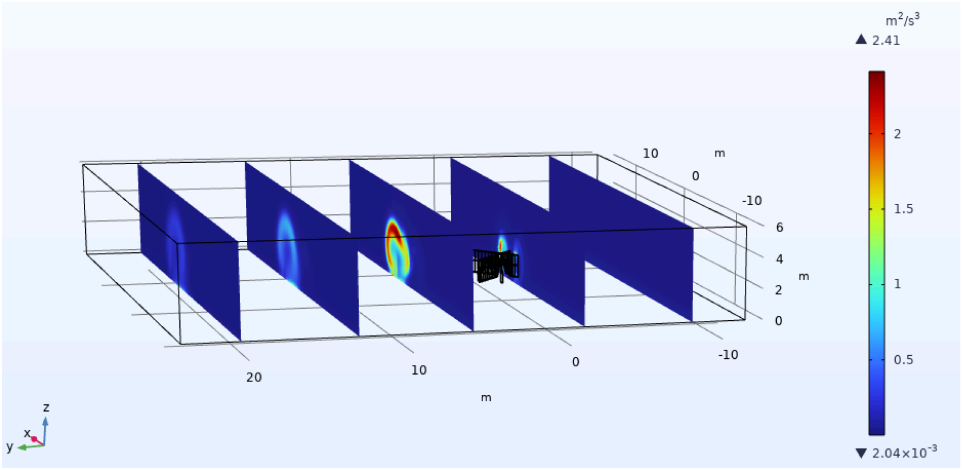


Figure 12. Dissipation fields of turbulent kinetic energy in five sections. For data, see Figure 7.

The range of change in excess pressure in the flow area at $\alpha = 0^{\circ}$ is $-8.93 \sim 17.4$ Pa. The areas of the highest and lowest pressures were formed, one might say, according to Bernoulli's law, with some deviations directly near the turbine (Figure 13). With the removal of the device downstream, the pressure field is intensively equalized.

The pressure contours (Figure 13) directly illustrate the fundamental driving mechanism of the turbine. A distinct high-pressure stagnation zone forms on the windward face of the closed "power-stroke" blades, coupled with a prominent low-pressure wake region behind them. This immense pressure differential generates the primary aerodynamic drag force that translates into positive shaft torque. Importantly, as the blades transition to the upwind "return stroke," their passive rotation mitigates the adverse high-pressure buildup that would otherwise oppose the turbine's rotation Figure 14. This dynamic pressure relief mechanism clearly explains the sustained positive power coefficient (C_p) and superior self-starting capabilities under low-wind conditions (3–5 m/s).

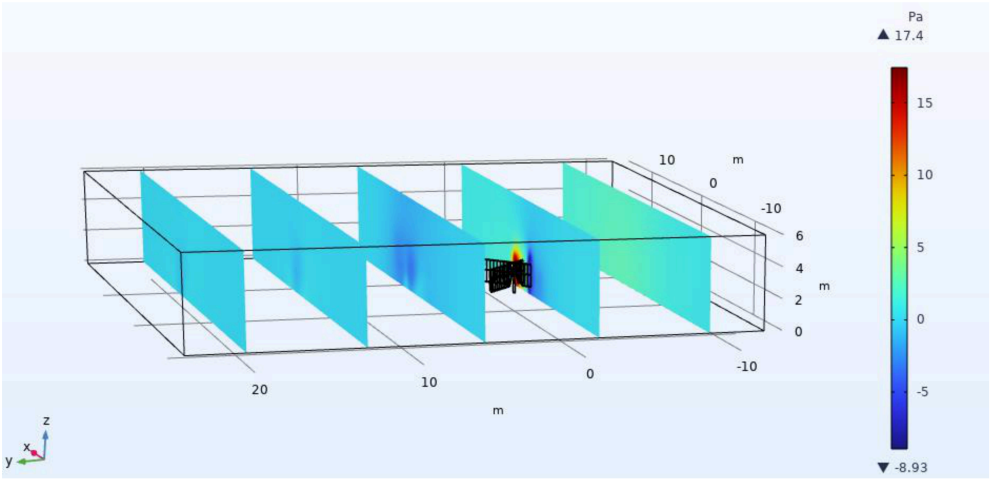


Figure 13. Pressure fields in five cross-sections. For data, see Figure 7.

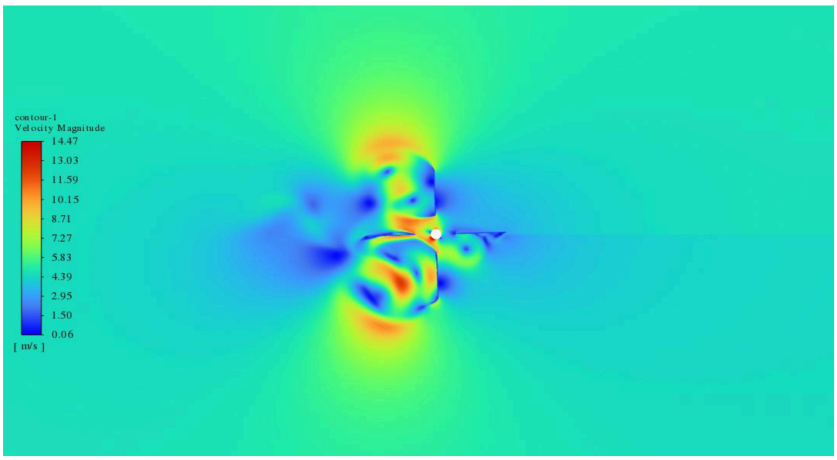


Figure 14. Velocity magnitude contour around the wind turbine profile at an inlet velocity of V = 8 m/s.

This factor is one of the main components of the resistance force and turbine efficiency. The results of this work showed that installing blades under the 25° spans leads to a complex flow pattern. At a distance of $x = -3.5$ m, the flow is already overpowered relative to the working areas of the harmful span. The main attachment of the velocity and pressure field occurs in the immediate vicinity of the device. Downstream, the pressure field is restored significantly faster than the fields of other indicators.

The identified parameters were theoretically investigated in terms of the turbine's motion under different wind speeds and the velocity fields formed around it. Since the turbine is installed at a high altitude, experimental investigations are technically challenging and economically costly; therefore, the process was analyzed using numerical modeling. Reducing the turbulent flow structures formed around the turbine improves aerodynamic efficiency and ensures stable operation. In addition, the resulting velocity values were evaluated as an important parameter for controlling the self-protection mechanism of the system.

The numerical contours in Figures 7–13 reveal distinct regions of negative velocity, particularly on the leeward side of the blades during the upwind-to-downwind transition. The physical origin of these negative velocity zones is attributed to the dynamic stall phenomenon and subsequent boundary-layer separation. At specific azimuthal angles, the effective angle of attack exceeds the critical stall limit of the airfoil, causing the flow to detach from the suction surface. This leads to the formation of a recirculation bubble where the flow direction reverses relative to the main stream. These flow reversal regions significantly

impact the turbine's performance by increasing the pressure drag and generating a negative torque contribution.

4. Experimental Methodology

In this section, experimental investigations were conducted to validate the numerical results and to assess their reliability. The purpose was to verify the actual performance of the newly developed vertical-axis wind turbine under low-wind-speed conditions in real environmental settings and to examine the selected optimal parameters. The experiments were performed using the currently developed prototype to evaluate its real operational characteristics.

The main objective of the experimental study was to identify possible deficiencies, improve the design based on the observed results, and enhance the feasibility of implementing the turbine in practical production. The obtained results serve as a basis for further optimization and confirm the practical application potential of the proposed turbine design.

Two main measurement devices were used during the experimental investigations. A calibrated cup anemometer was employed to measure and monitor the incoming wind speed, ensuring stable and repeatable flow conditions throughout the experiments. The anemometer provided real-time measurements of the inlet velocity during the tests.

In addition, a laboratory test bench equipped with magnetic holders was used to measure the mechanical characteristics of the vertical-axis wind turbine. This setup enabled the measurement of the rotational speed and the generated torque of the turbine shaft, providing experimental data for comparisons with the numerical simulation results Figures 15–18.



Figure 15. Vortex anemometer with wind speed indicator, data logger, and software.



Figure 16. Demonstration kit with magnetic holders for measuring the rotational speed and torque of the device.



Figure 17. Final configuration of the device and mast.



Figure 18. View of the device prepared for installation.

The performance of the turbine is evaluated using the power coefficient (C_p), which is a fundamental non-dimensional parameter representing the ratio of the extracted mechanical power to the available kinetic power of the incoming flow. This parameter plays a central role in the present study, as it serves as the primary metric for both numerical prediction and experimental validation of the turbine performance.

The use of the power coefficient allows the results to be expressed in a normalized form, making the performance evaluation independent of the flow velocity, turbine size, and operating conditions. Consequently, all comparative analyses in this work—including the assessment of different operating regimes and the validation of the numerical model—are based on the variation of C_p with respect to the tip speed ratio (λ) [36].

In [37], an experimental performance comparison was conducted between a conventional three-blade horizontal-axis wind turbine (HAWT) and an Ayanz-inspired screw-blade turbine under steady and transient urban wind conditions. The study revealed that while the three-blade turbine achieves a higher peak C_p, the Ayanz model exhibits a broader performance plateau and superior self-starting behavior in low and fluctuating wind environments. Furthermore, the authors introduced a 'plateau width analysis' framework for C_p vs. TSR curves to evaluate turbine adaptability and robustness to off-design conditions.

The numerical results demonstrate that the proposed novel vertical-axis wind turbine (VAWT) configuration exhibits high aerodynamic efficiency. Figure 19 illustrates the relationship between the power coefficient (C_p) and the tip speed ratio (TSR).

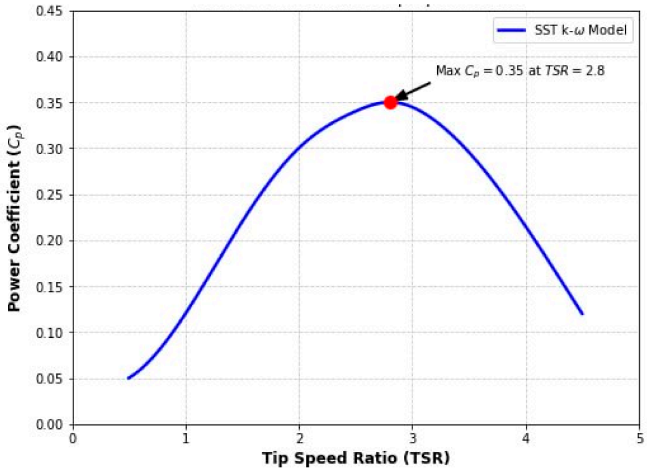


Figure 19. Variation in power coefficient (C_p) with tip speed ratio (TSR) for the proposed VAWT at 25° pitch angle.

As shown in the figure, the maximum power coefficient reaches C_p = 0.35 at an optimal tip speed ratio of TSR = 2.8. This performance level indicates that the proposed design is highly competitive with conventional Darrieus-type turbines used in the industry. This correlation was obtained using the SST turbulence model, which accurately captured the delayed flow separation at the 25° blade pitch angle, subsequently leading to an increase in the lift force. Furthermore, the turbine maintains a stable power output across a wide operational range, from TSR = 1.5 to 4.0, ensuring efficiency under fluctuating wind conditions.

Moreover, the power coefficient provides a direct and physically meaningful measure of the energy conversion efficiency of the turbine. Any improvement or degradation in turbine performance is therefore reflected through changes in C_p, making it an essential parameter for judging the reliability and accuracy of both the experimental measurements and the computational results.

Experimental investigations were carried out using the specialized experimental devices, and all measurement data and observations were obtained through these experimental setups. The performance of the turbine under real operating conditions was evaluated using these devices, and the collected data were analyzed and compared with the numerical simulation results.

The main result of this work is the determination of the total power of the wind generator at $\alpha = 0°$, as shown in Table 2.

Table 2. Power and thrust coefficients compared with experimental data.

Model	With$_p$
Standard k–ε	0.325
SST	0.347
RNG	0.326
k–ω	0.339
Experiment	0.356

To verify the reliability of the numerical simulation results, experimental investigations were conducted under controlled laboratory conditions. The experiments were

performed using a dedicated test bench designed to reproduce the operating conditions of the proposed vertical-axis wind turbine. The experimental setup consisted of a controllable airflow generation system, the turbine rotor coupled with an electrical generator, and data acquisition instruments.

The incoming wind speed was measured using a calibrated anemometer, and tests were carried out for wind velocities in the range of 3–8 m/s. The rotational speed of the turbine was measured using an optical or digital tachometer, while the generated torque and electrical power output were determined using appropriate torque sensors and electrical measurement devices. The output power was calculated based on measured voltage and current values.

Each experimental condition was repeated multiple times to ensure repeatability, and averaged values were used for comparison with numerical results. Measurement uncertainties were evaluated by considering the manufacturer-specified accuracy of the instruments and the statistical variation between repeated measurements. The overall uncertainty was estimated using standard error propagation methods applied to wind speed, rotational speed, torque, and electrical power measurements.

The experimental results were compared with the numerical predictions obtained from the CFD simulations. Key performance indicators, including torque and power coefficient, were used as comparison metrics. Good agreement between experimental and numerical results was observed, confirming the validity of the computational model and the chosen simulation parameters, as shown in Table 3.

Table 3. Comparison of power coefficients and relative errors with experimental data.

Model	Relative Error (%)
Standard k–ε	8.71
SST	3.37
RNG	8.43
k–ω	4.77
Experiment	0.00

Based on the comparison with experimental data, relative errors were calculated for each turbulence model. The SST model demonstrated the lowest deviation (3.37%), indicating the highest agreement with experimental results. Therefore, this model was selected as the most accurate for further analysis.

The main reason for choosing the SST model in this study was the need to more accurately represent the laminar–turbulent transition processes that occur at low Reynolds numbers. The conventional k–ε, RNG, and k–ω models cannot adequately represent these transitions, since they assume that the entire flow is completely turbulent. The transition model, on the other hand, allows for a physically based modeling of the fine boundaries between laminar, transitional, and turbulent regimes. In particular, it provides high accuracy in approximating the aerodynamic forces and flow separation zones around the blades under realistic conditions. Therefore, this model was considered superior in systems with complex flow dynamics, such as VAWTs.

Using turbulence models k–ε and SST to study the aerodynamics of a vertical wind turbine is a powerful approach to simulate complex air flows around the blades. The combined use of these approaches will not only increase the power factor but also improve the overall performance and reliability of the vertical wind turbine under various operating conditions.

Using the SST model, which has shown the best results in simulation, can indeed significantly improve the accuracy of developing a new vertical wind turbine model Table 4. The SST model is particularly effective in capturing complex aerodynamic phenomena such as shear flows and vortices that often occur around turbine blades.

Table 4. The highest and lowest values of longitudinal velocity in the flow region are given for different values of the angle α.

Corner α, Degree	**0**	**15**	**30**	**45**	**60**	**75**
U_{max} (m/s)	6.1	6.49	6.38	5.87	6.4	6.95
U_{min} (m/s)	−0.966	−0.605	−1.42	−3.25	−5.52	−6.66

The non-monotonic behavior of these indicators is associated with the braking effect of the working blades and their relative position at different values of the angle α. Comparisons of the highest and lowest transverse flow velocity in the flow region at different angle values α are shown in Table 5.

Table 5. The greatest and least transverse flow velocity in the flow region at different angle values α.

Corner α, Degree	**0**	**15**	**30**	**45**	**60**	**75**
V_{max} (m/s)	3.59	2.01	3.13	3.71	4.65	4.3
V_{min} (m/s)	−4.12	−4.06	−4.36	−4.99	−4.2	−3.96

At low wind speeds, the aerodynamic performance of the vertical-axis wind turbine is governed by complex flow phenomena, including flow separation, reattachment, and strong velocity and pressure gradients around the blade surfaces. The numerical results show that at wind velocities of approximately 3 m/s, localized flow separation occurs primarily on the leeward side of the blades, which directly influences the generated torque and overall power coefficient. However, the optimized blade geometry promotes early reattachment and limits the size of separation zones, thereby maintaining sufficient aerodynamic loading even under low incoming flow conditions.

The pressure distribution analysis reveals the formation of pronounced pressure differences between the upstream and downstream sides of the blades, which is a key mechanism driving rotor rotation at low wind speeds. Simultaneously, the velocity field indicates accelerated flow regions near the blade tips and moderate wake expansion downstream, suggesting efficient momentum extraction from the airflow. Turbulence intensity remains relatively localized near the blade surfaces, reducing excessive energy dissipation and contributing to improved efficiency in low-speed operation.

These aerodynamic characteristics explain the ability of the proposed turbine to operate effectively under low wind conditions. The interaction between controlled flow separation, favorable pressure gradients, and moderated turbulence levels enhances energy conversion efficiency, making the turbine particularly suitable for regions where wind speeds are consistently low. This analysis confirms that careful aerodynamic design and appropriate turbulence modeling are essential for achieving stable and efficient performance in low-wind-speed environments.

Figure 20 shows the electrical energy output of the new wind turbine with an improved working surface. The graph demonstrates that this turbine significantly outperforms existing analogues, as it is capable of operating at low wind speeds, allowing it to generate more energy compared to devices that begin power production only at higher wind speed values.

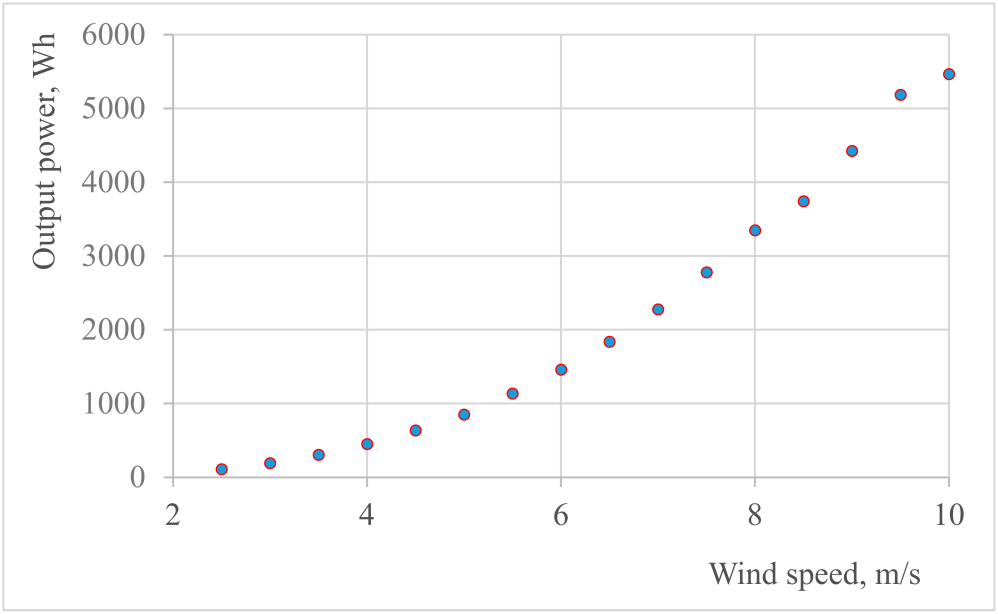


Figure 20. Wind turbine power curve.

5. Conclusions

This study presents a rigorous three-dimensional numerical investigation into the aerodynamic performance of a novel vertical-axis wind turbine (VAWT) specifically engineered for low-wind environments. By evaluating multiple turbulence models—including RNG k–ε, standard k–ε, k–ω, and SST—the following key conclusions were established.

Comparative analysis demonstrates that the SST (shear stress transport) model provides the highest degree of accuracy, exhibiting the closest agreement with experimental data. Its superior performance is rooted in its hybrid formulation, which effectively resolves the near-wall boundary layer using the k–omega approach while maintaining k–ε robustness in the far-field. This allows for precise capture of adverse pressure gradients and flow separation phenomena that are dominant in VAWT operations at low Reynolds numbers.

While the RNG k–ε model showed stability, it tended to overpredict turbulent viscosity, leading to an underestimation of separation zones. The standard k–ω model, though accurate near the blades, exhibited high sensitivity to free-stream conditions. The SST model's blending mechanism successfully mitigated these limitations, providing a high-fidelity representation of wake development and transient flow structures.

Validation against laboratory experiments confirms that the proposed turbine is capable of stable power generation at wind speeds as low as 3 m/s. The passive blade-pitch control mechanism significantly reduces negative torque on the return stroke, enhancing the net power coefficient (C_p) compared to fixed-geometry analogues.

Through the combined numerical and experimental approach, the optimal geometric and aerodynamic parameters were identified, establishing a reliable baseline for small-scale wind energy harvesting in urban and low-wind regions. In summary, the findings of this research provide a robust theoretical and empirical foundation for the development of highly efficient, sustainable energy technologies. The results offer valuable insights for the aerodynamic optimization of VAWTs, supporting the transition toward decentralized and environmentally friendly power generation systems.

Author Contributions: Conceptualization, I.K. and M.H.; methodology, I.K. and M.H.; software, M.H.; validation, I.K., M.H., O.T., J.T., B.W., Y.C., R.L. and Y.S.; formal analysis, M.H., B.W. and Y.S.; investigation, I.K. and M.H.; resources, O.T., J.T., R.L. and Y.S.; data curation, M.H. and Y.C.; writing—original draft preparation, M.H.; writing—review and editing, I.K., M.H., B.W. and Y.S.; visualization,

M.H. and Y.C.; supervision, I.K. and Y.S.; project administration, M.H. and R.L.; funding acquisition, O.T., J.T. and R.L. All authors have read and agreed to the published version of the manuscript.

Funding: The article was carried out with budget funding from the Institute of Mechanics and Seismic Stability of Structures named after. M.T. Urazbayev of the Academy of Sciences of the Republic of Uzbekistan.

Data Availability Statement: The data supporting the findings of this study are available from the corresponding author upon reasonable request.

Conflicts of Interest: Author Rongsheng Lin is employed by Jurong Energy (Xinjiang) Co., Ltd. The remaining authors declare that the research was conducted in the absence of any commercial or financial relationships that could be construed as a potential conflict of interest.

References

1. De Tavernier, D.A.M.; Ferreira, C.; Goude, A. Vertical-axis wind turbine aerodynamics. In *Handbook of Wind Energy Aerodynamics*; Stoevesandt, B., Schepers, G., Fuglsang, P., Yuping, S., Eds.; Springer: Cham, Switzerland, 2022. [CrossRef]
2. Hara, Y.; Moral, M.S.; Ide, A.; Jodai, Y. Fast Simulation of the Flow Field in a VAWT Wind Farm Using the Numerical Data Obtained by CFD Analysis for a Single Rotor. *Energies* **2025**, *18*, 220. [CrossRef]
3. Sun, X.; Zhu, J.; Hanif, A.; Li, Z.; Sun, G. Effects of blade shape and its corresponding moment of inertia on self-starting and power extraction performance of the novel bowl-shaped floating straight-bladed vertical axis wind turbine. *J. Sustain. Energy Technol. Assess.* **2020**, *38*, 100648. [CrossRef]
4. Devesse, K.; Lanzilao, L.; Jamaer, S.; van Lipzig, N.; Meyers, J. Including realistic upper atmospheres in a wind-farm gravity-wave model. *Wind Energy Sci.* **2022**, *7*, 1367–1382. [CrossRef]
5. Meneveau, C.; Shen, L.; Yang, D. Effect of downwind swells on offshore wind energy harvesting—A large-eddy simulation study. *Renew. Energy* **2014**, *70*, 11–23. [CrossRef]
6. Porté-Agel, F. A hybrid physics-based and data-driven model for intra-day and day-ahead wind power forecasting considering a drastically expanded predictor search space. *Appl. Energy J. Artic.* **2024**, *367*, 123375. [CrossRef]
7. Blocken, B.; Carmeliet, J.; Stathopoulos, T. Pedestrian-level wind conditions around buildings: Review of wind-tunnel and CFD techniques and their accuracy for wind comfort assessment. *Build. Environ.* **2016**, *100*, 50–81. [CrossRef]
8. Liu, Q.S.; Miao, W.P.; Li, C.; Hao, W.; Zhu, H.; Deng, Y. Effects of trailing-edge movable flap on aerodynamic performance and noise characteristics of VAWT. *Energy* **2019**, *189*, 116271. [CrossRef]
9. Rose, J.; Natarajan, S.G.; Gopinathan, V.T. Biomimetic flow control techniques for aerospace applications: A 485 comprehensive review. *Rev. Environ. Sci. Bio/Technol.* **2021**, *20*, 645–677. 486. [CrossRef]
10. Zhu, H.; Hao, W.; Li, C.; Ding, Q.; Wu, B. A critical study on passive flow control techniques for straight-bladed vertical axis 487 wind turbine. *Energy* **2018**, *165*, 12–25. [CrossRef]
11. Huang, S.; Qiu, H.; Wang, Y. Aerodynamic performance of horizontal axis wind turbine with application of dolphin head-shape and lever movement of skeleton bionic airfoils. *Energy Convers. Manag.* **2022**, *267*, 115803. [CrossRef]
12. Jiang, R.; Zhao, Z.; Liu, Y.; Liu, H.; Ma, Y.; Wang, T.; Feng, J.; Wang, D.; Li, S.; Luo, Q. Effect of vortex generator orientation on wind turbines considering the three-dimensional rotational effect. *Ocean Eng.* **2023**, *267*, 113307. [CrossRef]
13. Seel, F.; Lutz, T. Numerical study of the unsteady blade root aerodynamics of a 2MW wind turbine equipped with vortex generators. *Wind. Energy Sci. Discuss.* **2023**, *8*, 1369–1385. [CrossRef]
14. Zhang, Z.; Kuang, L.; Han, Z.; Zhou, D.; Zhao, Y.; Bao, Y.; Duan, L.; Tu, J.; Chen, Y.; Chen, M. Comparative analysis of bent and basic winglets on performance improvement of horizontal axis wind turbines. *Energy* **2023**, *281*, 128252. [CrossRef]
15. Damiola, L.; Siddiqui, M.F.; Runacres, M.C.; De Troyer, T. Influence of free-stream turbulence intensity on static and dynamic stall of a NACA 0018 aerofoil. *J. Wind Eng. Ind. Aerod* **2023**, *232*, 105270. [CrossRef]
16. Li, Y.; Wang, H.; Wu, Z. Aerodynamic characteristic of wind turbine with the leading edge slat and Microtab. *Sustain Energy Technol. Assess.* **2022**, *52*, 101957. [CrossRef]
17. Chen, D.; Xu, R.; Yuan, Z.; Pan, G.; Marzocca, P. The effect of vortex induced vibrating cylinders on airfoil aerodynamics. *Appl. Math. Model* **2023**, *115*, 868–885. [CrossRef]
18. Zaki, A.; Abdelrahman, M.A.; Ayad, S.S.; Abdellatif, O.E. Effects of leading edge slat on the aerodynamic performance of low Reynolds number horizontal axis wind turbine. *Energy* **2022**, *239*, 122338. [CrossRef]
19. Abbas, Z.; Waqas, M.; Saleem Khan, S.; Khatoon, R.; Larkin, S.; Zhao, L. Numerical and experimental investigation of an Archimedes screw turbine for open channel water flow application. *Energy Sci. Eng.* **2024**, *12*, 1317–1336. [CrossRef]
20. Menter, F.R. Zonal two equation kw turbulence models for aerodynamic flows. In *23rd Fluid Dynamics, Plasmadynamics, and Lasers Conference*; American Institute of Aeronautics and Astronautics: Reston, VA, USA, 2012; p. 2906. [CrossRef]

21. Menter, F.R.; Kuntz, M.; Langtry, R. Ten years of industrial experience with the SST turbulence model. *Turbul. Heat. Mass. Transf.* **2003**, *4*, 625–632.
22. Pasha, A.A. Study of parameters affecting separation bubble size in high speed flows using k–ω turbulence model. *J. Appl. Comput. Mech.* **2018**, *4*, 95–104. [CrossRef]
23. Toshov, Z.B.; Rahutin, M.G.; Toshov, B.R.; Baratov, B.N. Tracking prevention in roller cone bit drilling. *Eurasian Min.* **2024**, *2024*, 62–66. [CrossRef]
24. Toshov, J.B.; Rabatuly, M.; Bogzhanova, Z.K.; Zheldikbayeva, A.T.; Malikov, S.R.; Toshov, B.R.; Ergashev, O.S. Influence of Radiation and Magnetic Pulse Treatment on The Wear Resistance of Carbide Tools. *Complex Use Miner. Resour.* **2026**, *337*, 47–54. [CrossRef]
25. Malikov, Z.M.; Madaliev, M.E. Numerical study of a swirling turbulent flow through a channel with an abrubt expansion. *Vestn. Tomsk. Gos. Univ. Mat. I Mekhanika* **2021**, *72*, 93–101. [CrossRef]
26. Malikov, Z.M.; Madaliev, M.E. Mathematical modeling of a turbulent flow in a centrifugal separator. *Vestn. Tomsk. Gos. Univ. Mat. I Mekhanika* **2021**, *71*, 121–138. [CrossRef]
27. NASA. Turbulence Modeling Resource. Available online: https://turbmodels.larc.nasa.gov/naca0012_val.html (accessed on 19 May 2026).
28. Khujaev, I.; Jumayev, J.; Hamdamov, M. Modeling of Combustion Processes in Cylindrical Chambers Using Modern Package Programs. *AIP Conf. Proc.* **2024**, *3004*, 060015. [CrossRef]
29. Khujaev, I.; Toirov, O.; Jumayev, J.; Hamdamov, M. Modeling of vertical axis wind turbine using Ansys Fluent package program. *E3S Web Conf.* **2023**, *401*, 04040. [CrossRef]
30. Hamdamov, M.; Bozorov, B.; Mamataliyeva, H.; Ergashov, D. Numerical modeling of wind turbine with vertical axis using turbulence model k-ω in ANSYS FLUENT. *E3S Web Conf.* **2023**, *401*, 02024. [CrossRef]
31. Hamdamov, M.; Ishnazarov, A.I.; Mamadaliev, K. A Numerical Modeling of Vertical Axis Wind Turbines Using ANSYS Fluent Software. In *Internet of Things, Smart Spaces, and Next Generation Networks and Systems*; Lecture Notes in Computer Science (Including Subseries Lecture Notes in Artificial Intelligence and Lecture Notes in Bioinformatics); Springer: Cham, Switzerland, 2023; Volume 13772, pp. 156–170. [CrossRef]
32. Abul-Ela, M.S.; ElRefaie, M.E.; Sayed, A.I. Enhancing vertical-axis wind turbine self-starting with distinctive blade airfoil designs. *J. Eng. Appl. Sci.* **2025**, *72*, 95. [CrossRef]
33. Bystrov, D.; Olimjon, T.; Sanjar, G.; Mirzokhid, T.; Sardor, U. Role of Reengineering in Training of Specialists. In *ACM International Conference Proceeding Series NISS2020: Proceedings of the 3rd International Conference on Networking, Information Systems & Security*; ACM: New York, NY, USA, 2020; Article No. 49; pp. 1–4. [CrossRef]
34. Bystrov, D.; Olimjon, T.; Gulzoda, M.; Dilfuza, Y. Fuzzy Systems for Computational Linguistics and Natural Language. In *ACM International Conference Proceeding Series NISS2020: Proceedings of the 3rd International Conference on Networking, Information Systems & Security*; ACM: New York, NY, USA, 2020; Article No. 54; pp. 1–3. [CrossRef]
35. Abdi Yonis, S.; Yusupov, Z.; Habbal, A.; Toirov, O. Control approach of a grid connected DFIG based wind turbine using MPPT and PI controller. *Adv. Electr. Electron. Eng.* **2023**, *21*, 157–170. [CrossRef]
36. Gong, D.; Zhou, J.; Liu, X.; Li, F. Modeling and vortex-induced vibrations of semi-submersible floating offshore wind turbines. *Mech. Syst. Signal Process.* **2024**, *220*, 111667. [CrossRef]
37. Angulo, A.; Nazabal, U.; Rodriges, F.; Rojo, I.; Zarketa, A.; Cabezuelo, D.; Abad, G. Comparative Experimental Performance of an Ayanz Screw-Blade Wind Turbine and a Conventional Three-Blade Turbine Under Urban Gusty Wind Conditions. *Smart Cities* **2026**, *9*, 11. [CrossRef]
38. Khan, A.; Irfan, M.; Niazi, U.M.; Shah, I.; Legutko, S.; Rahman, S.; Alwadie, A.S.; Jalalah, M.; Glowacz, A.; Khan, M.K.A. Centrifugal Compressor Stall Control by the Application of Engineered Surface Roughness on Diffuser Shroud Using Numerical Simulations. *Materials* **2021**, *14*, 2033. [CrossRef] [PubMed]
39. Urbanowicz, K.; Bergant, A.; Stosiak, M.; Deptuła, A.; Karpenko, M. Navier-Stokes Solutions for Accelerating Pipe Flow—A Review of Analytical Models. *Energies* **2023**, *16*, 1407. [CrossRef]
40. Karpenko, M. Aircraft hydraulic drive energy losses and operation delay associated with the pipeline and fitting connections. *Aviation* **2024**, *28*, 1–8. [CrossRef]
41. Karpenko, M. Landing gear failures connected with high-pressure hoses and analysis of trends in aircraft technical problems. *Aviation* **2022**, *26*, 145–152. [CrossRef]

Disclaimer/Publisher's Note: The statements, opinions and data contained in all publications are solely those of the individual author(s) and contributor(s) and not of MDPI and/or the editor(s). MDPI and/or the editor(s) disclaim responsibility for any injury to people or property resulting from any ideas, methods, instructions or products referred to in the content.